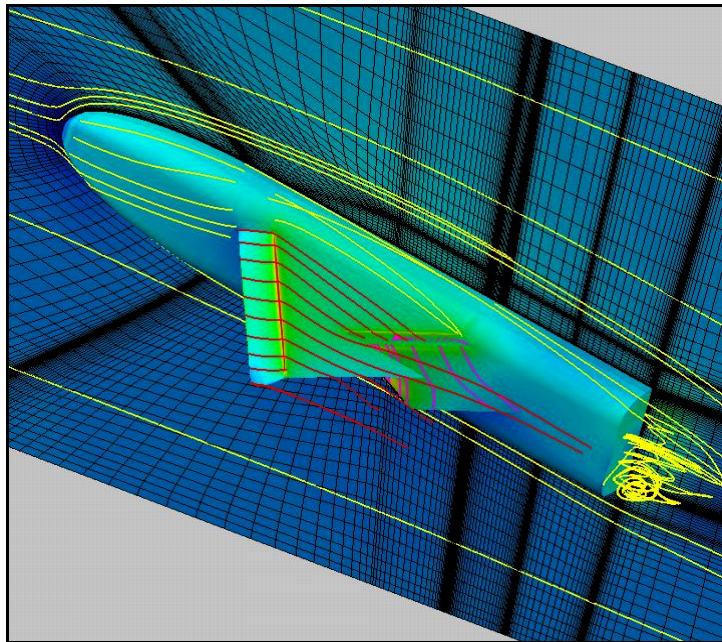




AIAA-2002-0846

***Numerical Viscous Flow Analysis of an
Advanced Semispan Diamond-Wing
Model at High-Lift Conditions***

***F. Ghaffari, R. T. Biedron and J. M. Luckring
NASA Langley Research Center
Hampton, Virginia***



***40th AIAA Aerospace Sciences Meeting & Exhibit
14-17 January, 2002
Reno, Nevada***

Numerical Viscous Flow Analysis of an Advanced Semispan Diamond-Wing Model at High-Lift Conditions

F. Ghaffari^{}, R. T. Biedron[§], and J. M. Luckring[†]*

NASA Langley Research Center
Hampton, Virginia

Abstract

Turbulent Navier-Stokes computational results are presented for an advanced diamond wing semispan model at low speed, high-lift conditions. The numerical results are obtained in support of a wind-tunnel test that was conducted in the National Transonic Facility (NTF) at the NASA Langley Research Center. The model incorporated a generic fuselage and was mounted on the tunnel sidewall using a non-metric/constant-width standoff. The analyses include: 1) the numerical simulation of the NTF empty tunnel flow characteristics, 2) semispan high-lift model with the standoff in the tunnel environment, 3) semispan high-lift model with the standoff and viscous sidewall in free air, and 4) semispan high-lift model without the standoff in free-air. The computations were performed at conditions that correspond to a nominal approach and landing configuration. The wing surface pressure distributions computed for the model in both the tunnel and in free air agreed well with the corresponding experimental data and they both indicated small increments due to the wall interference effects. However, the wall interference effects were found to be more pronounced in the total measured and the computed lift, drag and pitching moment due to standard induced up-flow effects. Although the magnitudes of the computed forces and moment were slightly off compared to the measured data, the increments due the wall interference effects were predicted well. The numerical predictions are also presented on the combined effects of the tunnel sidewall boundary layer and the standoff geometry on the fuselage fore-body pressure distributions and the resulting impact on the overall configuration longitudinal aerodynamic characteristics.

Nomenclature

BC boundary condition

* Research Engineer, Senior Member, AIAA

§ Research Scientist

† Senior Research Engineer, Associate Fellow, AIAA

Copyright © 2002 by the American Institute of Aeronautics and Astronautics, Inc. No copyright is asserted in the United States under Title 17, U. S. Code. The U. S. Government has a royalty-free license to exercise all rights under the copyright claimed herein for Governmental Purposes. All other rights are reserved by the copyright owner.

BL	boundary layer
b/2	reference semispan, 2.6927 ft
c	local chord, ft
C_D	drag coefficient, $Drag/q_\infty S_{ref}$
C_L	lift coefficient, $Lift/q_\infty S_{ref}$
C_m	pitching moment coefficient, pitching moment/ $q_\infty S_{ref} \bar{c}$
C_p	pressure coefficient, $p-p_\infty/q_\infty$
CFD	computational fluid dynamics
C-O	grid topology, C streamwise and O circumferential
c_{ref}	cruise wing reference chord at $y/(b/2)=0.3$, 3.295 ft
\bar{c}	wing mean aerodynamic chord, 3.143 ft
DERA	Defense Evaluation and Research Agency
FP	flat plate
H-H	grid topology, H streamwise and H spanwise
H-O	grid topology, H streamwise and O circumferential
LaRC	Langley Research Center
LE	leading edge
LEF	leading-edge flap
M_∞	free-stream Mach number
MIF	Model/standoff-In-Free-air
MIT	Model/standoff-In-Tunnel
MNIF	Model/No-standoff-In-Free-air
NASA	National Aeronautics and Space Administration
NTF	National Transonic Facility
OL	overlap, ft
p	local static pressure, psf
p_∞	free-stream static pressure, psf
q_∞	free-stream dynamic pressure, psf
RANS	Reynolds-Averaged Navier-Stokes
R_n	unit Reynolds number, per foot
$R_{\bar{c}}$	Reynolds number, based on \bar{c}
S_{ref}	wing reference semi-area, 6.5908 ft ²
SA	Spalart-Allmaras
TTCP	The Technical Cooperation Program
TE	trailing edge
TEF	trailing-edge flap
TS	tunnel station, ft
U/U_∞	ratio of local to free-stream axial velocity
WIC	wall interference correction
x/c	fraction of wing local chord
$y/(b/2)$	fraction of model semispan
XYZ	Reference coordinate system
α	angle of attack, degrees
α_c	corrected angle of attack for wall interference, degrees
y^+	inner law variable

Introduction

The high-lift flow and the resulting aerodynamics experienced by an aircraft in take-off and landing are some of the most complex and difficult phenomenon to simulate, either experimentally with wind-tunnel tests, or numerically with the computational fluid dynamics (CFD) methods. For an aircraft to achieve the high-lift levels, required during takeoff and landing, it typically deploys mechanical systems that are referred to as high-lift devices. These devices are usually comprised of leading and trailing edge flaps designed to maximize attached flow over the vehicle for acceptable aerodynamic lift, efficiency, and handling qualities. However, for high performance military aircraft (subject of the present study) this must be achieved within the context of a relatively low aspect ratio and thin wing, and thus the resultant high-lift flow field can vary considerably from that of conventional commercial transport configurations.

The numerical simulation of high-lift flows is very difficult because of the inherent geometrical complexity as well as the complex flow interactions that can occur. Such geometrical complexity introduced by high-lift devices includes physical gaps, cavity or cove regions, exposed flap side-edges that are often sharp, flap hinge-lines that may be sharp or rounded, etc. Progress has been made in recent years to numerically simulate the complex high-lift flow aerodynamics with Reynolds Average Navier-Stokes (RANS) formulations based on multi-block structured grid technology (Refs. 1-3) with various degrees of success. However, the geometrical complexity of the high-lift configuration often requires a tremendous amount of time and resources to be spent in grid generation to set up such a computation. An alternative approach based on the unstructured grid technology has received attention in the recent years (Refs. 4, 5), primarily because of its inherent flexibility in discretizing complex geometry. However, it is also widely believed that the existing unstructured grid technology, with capabilities to simulate the complex high-lift viscous flow characteristics, is still in the developmental stage and may not be ready for application by the general user community.

The present overall CFD plan, shown schematically in Fig. 1, has two main objectives. The first objective is to calibrate a state-of-the-art RANS method for predicting the low-speed high-lift aerodynamics of an advanced high performance military wing concept recently tested in the NTF (Ref. 6) at the NASA Langley Research Center (LaRC). The semispan wind-tunnel model was designed as part of a multi-national collaborative effort (Ref. 7) under the auspices of The Technical Cooperation Program (TTCP). TTCP participants involved in this effort included the United

States Department of Navy, National Aeronautics and Space Administration (NASA), and the United Kingdom Defense Evaluation and Research Agency (DERA). The model incorporated a generic fuselage and was mounted on the tunnel sidewall using a constant width standoff.

For the present code calibration purposes, the CFD model included not only the semispan configuration but also the wind tunnel solid walls representing the NTF test section environment. The focus of the present numerical analysis is on the high-lift configuration with a specific rigging arrangement designed for approach landing conditions. These computations include an empty tunnel simulation to calibrate the viscous sidewall flow (Fig. 1a) and then a simulation of the model-in-tunnel configuration (Fig. 1b).

The second objective of this study is to numerically assess the interference effects due to the wind-tunnel walls and the standoff geometry for this configuration. This is accomplished numerically through a systematic removal of wall interference effects due to solid-wall confinement (Fig. 1c) and due to viscous sidewall and standoff combination (Fig. 1d). Experimental wall interference effects were also obtained, and these are used to help assess the numerical results. The present analysis on this slender vehicle also contributes to the ongoing activities, both experimentally (Ref. 8) and numerically (Ref. 9) at LaRC to develop a semispan test capability at the NTF, which have been primarily focused on commercial transport configurations.

Wind-tunnel model and test description

The semispan wind-tunnel model consisted of a generic fuselage with a 1.5-inch non-metric/constant-width standoff and a cropped diamond wing planform with leading and trailing edge sweep of 40° and -40° , respectively. The wing was designed for multi-mission interdisciplinary military requirements for cruise, high angle of attack maneuver, as well as for low-speed, high-lift performance. The photographs in figure 2 show the high-lift version of the model from two different perspective views. The wing consisted of a full span leading-edge flap, a part-span slotted trailing-edge flap, and a deflectable shroud ahead of the trailing-edge flap. The semispan model was mounted on the tunnel sidewall by including a constant width standoff designed to minimize the sidewall boundary layer (BL) effects on the model aerodynamics. The primary purpose of the test was to develop an experimental database for four different variations of the diamond wing with respect to the flap rigging arrangements (gap and overlap). These configuration variations included two high-lift riggings for approach and landing, one high-lift rigging for take-off, and the baseline cruise-model with no control surface deflections. Data from this experiment include

static surface pressures, configuration (i.e., wing and fuselage combination) forces and moments, and aeroelastic deformations for many high-lift settings.

The semispan model was 7.7 ft long and 2.7 ft wide excluding the 1.5-inch constant width standoff. The entire test was conducted in the air mode mainly because the model was designed for tests at elevated pressures; the combination of model size and pressure produced full-scale Reynolds number data. The model was instrumented with approximately 450 orifices to measure the surface pressures. The majority of the pressure orifices were distributed over the wing and in particular around the high-lift system. The wing pressure orifices were primarily distributed along six chord-wise stations located at $y/(b/2)=0.15, 0.30, 0.45, 0.55, 0.70,$ and 0.80 (Fig. 3)

The high-lift wing configured for approach and landing was chosen as the baseline configuration for the present numerical analysis. The high-lift control surfaces for this baseline configuration included a 22° deflected full-span leading-edge flap (LEF), 23° deflected shroud, and 35° deflected trailing-edge flap (TEF). In addition, the selected baseline model incorporated a $0.5\%c_{ref}$ gap and a $2\%c_{ref}$ overlap rigging (Fig. 4) arrangement. Representative flow conditions for approach and landing were also selected for the numerical analysis and they are $\alpha=10^\circ$, $M_\infty = 0.2$, $R_{ft}=7.7 \times 10^6$. For reference, the selected unit Reynolds number of 7.7×10^6 corresponds to the Reynolds number of 24.2×10^6 based on the wing mean-aerodynamic chord. Limited aerodynamic analysis of the experimental data has been reported in Ref. 10.

Computations and flow field analysis

The present numerical analysis is performed with the Multi-block, structured-grid based CFD code known as CFL3D (Ref. 11). The code is well documented and has been extensively calibrated for variety of applications with different classes of flows and configurations (Refs. 12-15). The algorithm is based on the compressible, time-dependent, Reynolds-averaged Navier-Stokes equations that are written in a curvilinear coordinate system. A cell-centered, finite volume approach is used to solve the equations in a conservative form. An upwind-biased, flux-difference-splitting (Ref. 16) is used to solve the inviscid terms whereas central differencing is applied to solve the viscous terms. The present numerical results are all based on the one-equation model of Spalart-Allmaras (Ref. 17). The solutions presented in this report are all obtained by the use of multi-gridding and multi-sequencing techniques to accelerate the convergence characteristics. The various grid-block interfaces in the physical domain are connected to one another either in a two-dimensional planar form or a three-dimensional non-planar form. The

flow primitive variables are interpolated across the various block interfaces using a searching technique based on a combination of linear and polynomial equations as discussed in Ref. 18.

Empty tunnel flow simulation

The empty tunnel flow simulation was conducted primarily for two reasons. The first reason was to establish that the tunnel sidewall BL could be reasonably simulated. The second reason was to determine whether a mixed viscous and inviscid boundary condition for modeling the tunnel walls was adequate to simulate the test section flow field.

The initial numerical model included only the nominal NTF test section and the tunnel sidewall was treated with a viscous boundary condition whereas the other three walls were simulated with an inviscid boundary condition (Fig. 5). The characteristic inflow BC and the outflow BC with specified pressure ratio (p/p_∞) of 1.0 were imposed at the tunnel inlet and exit plane, respectively. The BL rake data (Ref. 19) measured at tunnel sidewall station 13 ft (at the model center of rotation, see Fig. 5) are used to assess the accuracy of the numerical predictions. The rake was 6.25 inches tall and incorporated 29 probes with the first 8 probes distributed uniformly over the first inch to measure the near field pressure normal to the sidewall. The rake data analysis indicated that the edge of the BL (i.e., $U/U_\infty = 0.99$) occur at height of ~ 3.8 inches (~ 96.52 mm).

Four sets of Cartesian grids (i.e., H-H topology) were generated with different grid resolution to address grid sensitivity effects on the results. Complementary to the BL rake data, computations were performed at $M_\infty = 0.2$, and $R_{ft} = 2 \times 10^6$, based on the Reynolds-averaged Navier-Stokes (RANS) formulation with Spalart-Allmaras (SA) turbulence model. The correlation of these computed results with the measured BL thickness (see fig. 6) indicated an expected disagreement because the numerical model did not include a proper BL profile at the inflow plane.

Due to the simplicity of the tunnel sidewall BL simulation, it was decided to exploit flat-plate (FP) theory for estimating the BL thickness growth along the tunnel sidewall. The flat-plate theory estimates (buried under the open symbols) of the BL thickness growth were found to be very close to the turbulent Navier-stokes results computed for the nominal NTF test section (see Fig. 6). As a result, it was decided to use the flat-plate BL theory and the existing experimental data point (i.e., BL height of 3.8 inches (96.52 mm) at TS-13) to extrapolate a virtual origin to the NTF test section that would provide a better approximation of the BL thickness at TS-13. The tunnel virtual origin was

determined (Fig. 6) from this analysis to be approximately 15 ft (4600 mm) ahead of the nominal NTF test section.

Finally the accuracy of the estimated NTF virtual origin by the flat-plate theory was verified by applying the turbulent (SA) Navier-Stokes method. This calibration was performed by modifying the volume grid generated earlier for the computation of the nominal NTF test section (i.e., 65-axial, 129-normal to the sidewall, 65-lateral, $y^+ \sim 0.9$) to accommodate grids for the upstream extension of the tunnel geometry. The turbulent Navier-Stokes results for the BL height growth along the extended NTF sidewall is also shown in figure 6. The Navier-Stokes results for the extended NTF sidewall clearly reaffirm that the flat-plate BL height estimates were very reasonable. It should be noted that with this approach the relatively complex contraction-cone and the settling-chamber geometry are essentially replaced with a simple linear upstream-extension of the square cross-section, tunnel geometry.

The measured velocity profile along with the axial velocity profiles computed for the nominal and the extended NTF test section were also examined. Though not presented here, the comparison clearly illustrated an excellent agreement between BL rake measurements and the computed velocity profile with the extended NTF test section. In addition, as part of the NTF empty-tunnel flow simulation study, turbulent (SA) Navier-Stokes computations were also carried out by simulating the viscous BL flow on all four walls of the extended tunnel geometry. The results from this study revealed that only a slight thinning of the sidewall BL occurred and that it did not manifest itself until reaching TS 5 ft. This thinning of the BL thickness was computed to be approximately 0.1 inch (less than 3% of the overall BL thickness) at TS 13 ft. The empty tunnel flow simulation study provided sufficient insight into the tunnel flow characteristics (i.e., establishment of a tunnel virtual origin and the proper resolution of sidewall BL characteristics) that can directly be applied to the flow simulation over the semispan diamond wing model in the tunnel.

Model/standoff-In-Tunnel (MIT)

This section includes discussion on the computational grid, numerical solution development and typical flow field results.

A multi-block structured-grid was developed to discretize the semispan high-lift diamond wing model with the standoff geometry in the nominal NTF test section (see Fig. 7). The high-lift brackets (Fig. 2) were not modeled in the present numerical analysis, because of: 1) the added grid generation complexity, 2) their

presence should not have a significant impact on the overall configuration aerodynamics. The semispan diamond wing numerical model is rotated geometrically and set at 10° angle-of-attack with respect to the tunnel free-stream. Provisions were made from the empty tunnel flow simulation to properly size the grid over the viscous sidewall and to accommodate the tunnel upstream block extension (not shown in Fig. 7). Same inflow and out flow BC as those used in the empty tunnel flow simulations were imposed at the tunnel inlet and exit plane, respectively. Viscous BC was invoked on all lifting surfaces of the model with the exception of the fuselage base. Inviscid BC was imposed on the fuselage base to alleviate any possible convergence difficulties due to the expected complexity of the flow field (i.e., unsteady, turbulent wake flow field). In addition, the contribution of the fuselage base to the overall configuration forces and moment will be subtracted for subsequent analysis; this is consistent with the experimental data. The volume grid consisted of 39-grid blocks and containing approximately 7 million grid points.

The XYZ reference coordinate system for the grid is defined such that: positive X is from upstream to downstream, positive Y is normal to the sidewall, and positive Z is from tunnel ceiling to floor. The volume grid is defined in metric units where the viscous sidewall is located at $Y = -1.5$ inch (i.e., -38.1 mm standoff width) with the opposing side at $Y = 8.077$ ft (i.e., $Y = 2461.9$ mm). The overall longitudinal length of the nominal NTF test section is defined to be 25 ft (i.e., 7620 mm) long.

A close-up view of the surface grid for the semispan diamond wing model along with the tunnel sidewall grids is shown in Fig. 8. The complexity of the geometry and the care taken to resolve the cove and the gap regions are clearly illustrated. The inboard edge of the deflected TE flap is abutted against the fuselage whereas the outboard side-edge is exposed to the flow.

Turbulent Navier-Stokes computations were performed by setting the tunnel free-stream conditions to $M_\infty = 0.2$, $R_{ft} = 7.7 \times 10^6$, and at zero degree angle-of-attack. However, note that the angle of attack (α) for the model is 10° , because as discussed previously, the geometrical model is rotated to 10° angle of incidence relative to the tunnel free-stream condition. A solution convergence procedure was developed for this baseline MIT case that could be applied in a consistent way to the other cases in the present investigation.

With this procedure, the overall solution convergence was achieved using three grid levels (i.e., coarse, medium, and fine). Over the course of this solution development, the overall residuals were reduced by about

2.5 orders of magnitude and the oscillations in the computed total lift, drag, and pitching moment were reduced to a negligible level. Over the last 500 iterations of the fine grid solution, the average variations in total lift, drag, and pitching moments were found to be $\pm 0.07\%$, $\pm 0.13\%$, and $\pm 0.3\%$, respectively. Figure 9 shows the overall solution convergence history that took about 60 hours of Cray C-90 and required about 300MW of memory. Figure 9 also shows a more quantitative variation of the residuals for each block during the course of the solution development at every 1000 iteration intervals.

A composite image summarizing the computed flow field in terms of pressure coefficient for the MIT case is shown in Fig. 10. The surface pressure coefficients are shown on the semispan diamond wing model, tunnel sidewall, inflow/outflow and the floor plane of the upstream portion of the extended NTF test section. In addition to the surface pressure coefficients, the results in Fig. 10 show traces of several particles released in the field near the tunnel sidewall just ahead of fuselage and around the leading edges of the wing and the trailing edge flap. A few particles were also released close to the fuselage blunt base to highlight the associated wake flow-field structure. The particle traces are computed without any restriction to a particular computational grid plane. The computed flow characteristics generally show the desired attached flow, from a high-lift design stand point, over the LEF, main wing, shroud, and TEF for the most part. The close-up image on the upper right corner of the figure shows the low-pressure footprint associated with the TEF side- flow separation forming a vortex (off surface structure not shown here).

Model/standoff-In-Free-air (MIF)

The grid strategy chosen for the MIF computations utilized the existing MIT grid without any alteration. The MIF grid required six new grid blocks to extend the MIT tunnel walls to the nominal far field (see Fig. 11). The radial extent of the far-field boundary was chosen to be about five overall fuselage body-lengths (i.e., $12.2\bar{c}$) away from the tunnel centerline. These six blocks added a total of approximately 160,000 points to the existing MIT volume grid.

The identical procedures developed to obtain the turbulent Navier-Stokes solutions for the MIT case were applied to acquire the computational results for the MIF case at the same flow conditions. The MIF solution convergence characteristics and the resulting flow features were almost indistinguishable from those of the MIT case shown earlier in Figs. 9 and 10, respectively. As a result, they are not presented here.

Model/No-standoff-In-Free-air (MNIF)

The volume-grid blocks associated with the standoff were extracted from the existing MIF computational grid. This modification resulted in a total of 38 grid blocks, and about 6.5 million grid points, to remain for the numerical representation of the model/no-standoff in free-air (MNIF). The same boundary conditions as the MIF case were applied on all surfaces with the exception of the configuration plane-of-symmetry where the general symmetry plane boundary condition was imposed. The computational procedure established under the MIT and MIF solution development were applied to obtain the turbulent Navier-Stokes solution for the MNIF case at $\alpha = 10^\circ$, $M_\infty = 0.2$, and $R_{ft} = 7.7 \times 10^6$.

Predictions and correlation with data

Two sets of experimental data, referred to as ‘with WIC’ and ‘without WIC’, will later be presented in this report. While both data sets include all the standard wind-tunnel data corrections, the only difference between them is that one contains the experimentally determined solid-wall interference correction (Ref. 20) effect and the other does not. The application of WIC to correct the experimental data that corresponds to the flow conditions chosen for the numerical analysis resulted in an increase in the model angle of attack, free stream Mach number, and dynamic pressure. The corresponding increments in angle of attack (10°), free-stream Mach (0.2) and dynamic pressure (347.6 psf) were 0.6° , 0.001, and 4.54 psf, respectively. With the exception of the angle of attack, the increments to Mach number and dynamic pressure are considered relatively small in the present investigation. To numerically complement the corrected experimental data, an additional MIF computation was performed at $M_\infty = 0.2$, $R_{ft} = 7.7 \times 10^6$, and a higher free-stream angle-of-attack of 0.6° . As a result, the corrected angle of attack (α_c) for the numerical model (rotated to 10° angle of incidence relative to the tunnel free-stream flow) in this new computation is 10.6° . The results from this new MIF computation at $\alpha_c = 10.6^\circ$, along with those originally planned will be later correlated with the corresponding experimental data for surface pressure coefficients and overall forces and moment.

Surface pressure coefficients

The computed surface pressure coefficients, the NTF data (both with and without corrections for wall interference effects), and the wing geometry sectional cuts at three span-wise stations are shown in Fig. 12. The experimental data are only shown for the wing main element because of the inconsistencies found in mapping the experimental pressure-port locations with

the corresponding CFD data over the shroud and the TEF. The CFD results are shown for four different cases that include the MIT, MIF, MNIF, and the MIF at $\alpha_c = 10.6^\circ$ along with the NTF experimental data. The latter experimental data are shown for both corrected (denoted by ‘with WIC’) for the tunnel wall effects to represent the free-air results and uncorrected (denoted by ‘without WIC’) for the tunnel wall effects. In general, the pressure distributions computed over the main wing compare well with the measured data for the model in both the tunnel and free-air, and that they both indicate very little increment due to the wall interference effects. Similar chord-wise pressure distributions and the corresponding geometry sectional cuts, as shown in the previous figure, are presented in Fig. 13 for the three wing outboard-stations. Note that the experimental data are shown for the entire wing section and do not include any high-lift element. Similar to the wing inboard stations, the WIC modification to account for the tunnel wall effects on the measured surface pressures appears to be very small. The CFD results for the MIT and MIF show small variations in the computed pressures around the leading edge of the deflected flap. The agreement between the CFD results and the measured data are generally very good at all three stations.

Force and moment coefficients

The computed overall lift, drag, and pitching moment coefficients are shown in Fig. 14 along with the corresponding NTF experimental data with and without WIC application. The close-up views of each respective data set near the flow conditions of interest to the present investigation are shown in the right-hand column. *Consistent with the experimental data, it is important to note that the direct contributions from the standoff geometry and the blunt fuselage-base are excluded from all the computed coefficients.* The experimental lift coefficients indicate a fairly linear variation with angle-of-attack and the application of WIC to account for the tunnel wall interference results in a decrease in lift curve slope as expected. The computed lift coefficients from the MIT and MIF agree well with the measured data, especially the increments due to WIC (see the close-up results). The overall magnitudes are slightly over-predicted by about 0.01. Also the MIF computed lift coefficient at $\alpha_c = 10.6^\circ$ correlates well with the NTF data with WIC. As a result, the lift curve slope for the free-air computations (i.e., MIF and MIF at $\alpha_c = 10.6^\circ$) is also predicted well. Extracting the standoff geometry physically from the numerical model causes only a small decrease in the MNIF computed lift coefficient relative to the MIF

prediction and it compares very well with the corrected (i.e., wall interference effects) NTF data.

The measured pitching moment characteristics exhibit very little change at low to moderate C_L range, followed by a nose down tendency with increasing C_L . The experimental data also indicate diminutive effects from the application of WIC method on the overall pitching moment characteristics. The correlation of the computed pitching moments with experimental data is reasonable, though the plot on the right-hand column may be misleading because of the expanded scales.

The measured drag polar indicates the expected trend and that the modification due to WIC application appears to become more pronounced with increasing C_L . The computed drag coefficients are in general agreement with the experimental measurements in terms of the trends but not the magnitude. Also note the increase in the predicted drag coefficient (~55 counts) with MNIF computation compared to the MIF result. In addition to the obvious geometrical differences between the two models (i.e., standoff), there is also the imposed boundary condition on the configuration plane-of-symmetry. In an effort to determine a possible source for this drag change, further diagnostic analysis was performed as discussed in the following section.

Sidewall/standoff interference analysis

The predicted drag coefficients from MIF and MNIF computations are shown in Fig. 15 along with the results for the other two CFD cases for completeness. The drag coefficients are plotted against the block number in the computational domain. The results indicate that the computed drag remains fairly unchanged for most the blocks with the exception of the first two that define the configuration forebody longitudinally up to the fuselage/wing-LE juncture point. The majority of the increase in MNIF computed total drag, relative to MIF results, come from the configuration forebody (roughly about 40 counts) and the wing components (roughly about 10 counts). The effect over the forebody is likely to be associated with the standoff geometry and the boundary condition imposed on the wall to which the model is mounted, i.e., viscous wall for MIF and symmetry plane for MNIF. As a result, the configuration forebody experiences a different flow-field surrounding MIF computations compared to the MNIF. This forebody drag increment could be important to the process of estimating full span aerodynamics from semispan measurement. Similar data analysis was also performed for the computed lift coefficients that indicated negligible variations in all blocks with the exception of the wing components, which showed slight variations.

Computed pressure distributions along the fuselage centerline (i.e., fuselage and standoff boundary line, $Y=0$ mm) are shown in Fig. 16. The results clearly indicate very small differences between all the computations with the exception of the MNIF solutions over the configuration forebody. The majority of the differences occur roughly over the front one-third of the fuselage where the MNIF predicted pressures appear to exhibit less suction on the upper surface and more compression on the lower surface. As expected, only the computed pressure coefficients with MNIF indicate a stagnation point (i.e., $C_p \sim 1.0$) on the forebody unlike all the other solutions where their respective pressure coefficients do not exceed 0.83. The bulging of the pressure distribution in the mid-fuselage region ($0 < X < 1200$) is attributed to the wing pressure field propagation inboard onto the fuselage. It is also interesting to note that the fuselage pressure distributions indicate a rapid decrease and increase in pressures, near the fuselage base on the upper ($X \sim 1700$ mm) and lower surfaces ($X \sim 1600$ mm), respectively. This abrupt change in the fuselage pressure difference near the base plane is likely caused by the flow separation at the sharp corners of the base resulting in a wake-like flow-field behind the blunt face of the fuselage. The cross sectional pressure distribution on the forebody is analyzed next to identify the circumferential extent of the pressure difference between MNIF and the other CFD results. The computed circumferential pressure distribution at two fuselage cross sections of $X = -500$ mm and $X = -200$ mm are shown in Fig. 16. The first cross section is very close to the fuselage nose (see Fig. 16 for relative location with respect to the overall fuselage length) and the second station is roughly about the mid-forebody. The figure also shows the corresponding cross-sectional geometry including the standoff component (hash-marked) for reference. The results clearly indicate that the pressure difference observed between the MNIF and the other CFD solutions on the forebody is not confined to the fuselage centerline but it also manifests itself circumferentially at both stations. Similar to the earlier findings, the computed forebody pressures from the MIT, MIF, and MIF (at $\alpha_c = 10.6^\circ$) cases show very little difference between one another. It is important to recall that the computed wing pressures did not change significantly between all the examined CFD cases. The combination of the viscous sidewall and standoff certainly has a much larger effect on the forebody pressures compared with the MNIF predictions. The differences in forebody pressures are large enough to impact the computed drag coefficient (Fig. 16).

Complementary to the surface pressure comparison at the fuselage centerline (i.e., Fig. 16), figure 17 shows

the difference in the computed pressure coefficients at the plane-of-symmetry between the MIF and MNIF solutions. The grids are shown for every three points in both directions for clarity. This result clearly shows the field effect due to the presence of the combined sidewall BL and standoff geometry across the fuselage centerline plane. Similar to the earlier findings, this result also indicates that the majority of the pressure difference between the two solutions is confined only *in and around the forebody region* such as the flow compression ahead of the forebody followed by the flow expansion around it. These findings are consistent with the approach taken to design the standoff shape (Ref. 9) around the fuselage forebody to minimize the sidewall BL impact over the configuration flow field and thus measured aerodynamic properties.

Conclusions

Turbulent (Spalart-Allmaras) Navier-Stokes computational results are presented for an advanced diamond wing semispan model at low speed, high-lift conditions. The numerical results are obtained in support of a wind-tunnel test that was conducted in the National Transonic Facility (NTF) at the NASA Langley Research Center. The diamond wing model incorporated a generic fuselage and was mounted on the tunnel sidewall using a non-metric/constant-width standoff. The computations are performed at flow conditions of $\alpha = 10^\circ$, $M_\infty = 0.2$, and $R_{ft} = 7.7 \times 10^6$ that corresponded to a nominal flight approach and landing situation. The overall CFD plan included the numerical simulation of the NTF empty tunnel flow characteristics, semispan high lift model with the standoff in the tunnel environment, semispan high-lift model with the standoff and viscous sidewall in free-air, and semispan high-lift model without the standoff in free-air.

At the outset, the numerical analysis demonstrated an approach to determine an upstream extension (virtual origin) to the nominal NTF test section for better simulation of the empty-tunnel sidewall boundary-layer characteristics. The lessons learned from the empty tunnel flow simulation were then applied to simulate flow over the complete high-lift model in the tunnel and free air environment. The numerical predictions showed very little wall interference effect on the local flow characteristics of the model, which exhibited the desired attached flow over the LEF, main wing, shroud, and the TEF for the most part. The computed wing pressure distributions are shown to agree well with the measured data and they both indicate a small effect due to the tunnel wall interference effects. Although the magnitudes of the computed forces and moment were

slightly off compared to the measured data, their increments due the wall interference effects are predicted well. Numerical predictions for the combined effects of the tunnel sidewall boundary layer and the standoff geometry are shown to significantly impact the fuselage forebody pressure distribution. As a result, this effect is shown to influence the overall configuration longitudinal aerodynamic characteristics, particularly the drag coefficient, for the model with no standoff in free air.

Acknowledgement

The authors would like to thank Michael Wiese, Norma Bean, and Douglas Nark of Analytical Services and Material, Inc. for their grid generation effort. The authors would also like to thank Chip Bobbitt, Jr. and Joel Everhart of NASA LaRC for providing the NTF empty tunnel boundary layer rake data and the experimental wall interference effects for the diamond wing test, respectively.

References

1. Takallu, M.A., Laflin, K.R.: Reynolds-Average Navier-Stokes Simulations of Two Partial-Span Flap Wing Experiments. AIAA Paper No. 98-0701, January 1998.
2. Berkman, M.E., Khorrami, M.R., Choudhari, M., Sadowski, S.S.: Investigation of High-Lift Flow Field of an Energy Efficient Transport Wing. AIAA Paper No. 99-0926, January 1999.
3. Rogers, S.E., Roth, K., Cao, H.V., Slotnick, J.P., Whitlock, M., Nash, S.M., Baker, M.D.: Computation of Viscous Flow for a Boeing 777 Aircraft in Landing Configuration. AIAA Paper No. 2000-4221,
4. Mavriplis, D.J., Pirzadeh, S.: Large-Scale Parallel Unstructured Mesh Computations for 3D High-Lift Analysis. AIAA Paper No. 99-0537, January 1999.
5. Ghaffari, F.: Unstructured Grid Viscous Flow Simulation Over High-Speed Research Technology Concept Airplane at High-Lift Conditions. NASA/TP-1999-209718, November 1999.
6. Wahls, R. A.: The National Transonic Facility: A Research Retrospective (Invited). AIAA Paper No. 2001-0754, January 2001.
7. Luckring, J.M., Ghee T.A.: Subsonic Reynolds Number Effects on a Diamond Wing Configuration (Invited). AIAA Paper No. 2001-0907, January 2001.
8. Gatlin, G.M., Parker, P.A., and Owens, Jr., L.R.: Development of a Semispan Test Capability at the National Transonic Facility (invited). AIAA Paper No. 2001-0759, January 2001.
9. Milholen II, W. E.: A Design Methodology for Semispan Model Mounting Geometries. AIAA Paper No. 98-0758, January 1998.
10. Ghee, T.A. and Taylor, N.J.: Low-speed Wind Tunnel Tests on a Diamond Wing High-Lift Configuration. AIAA Paper No. 2000-4504.
11. Krist, S. L., Biedron, R. T., and Rumsey, C. L.: CFL3D User's Manual (Version 5.0), NASA TM-1998-208444, June 1998.
12. Vatsa, V.N., Thomas, J.L., and Wedan, B.W.: Navier-Stokes Computations of Prolate Spheroids at Angle of Attack. AIAA Paper No. 87-2627, August 87.
13. Thomas, J.L., Walters, R.W., Taekyu, R., Ghaffari, F., Weston, R.P., Luckring, J.M.: A Patched-Grid Algorithm for Complex Configurations Directed Towards the F/A-18 Aircraft. AIAA Paper No. 89-0121, January 1989.
14. McMillin, S. N., Thomas, J. L., Murman, E.M.: Navier-Stokes and Euler Solutions for Lee-Side Flows Over Supersonic Delta Wings — A correlation With Experiment. NASA TP-3035, 1990.
15. Ghaffari, F., Luckring, J. M., Thomas, J. L.: An Overview of the Navier-Stokes Computations About the F/A-18 Aircraft With Multiblock Structured Grids. Proceedings from High-Angle-of-Attack Technology, Accomplishments, Lessons Learned, and Future Directions. NASA Langley Research Center, Sept. 17-19, 1996. NASA/CP-1998-207676/PT3, pp. 1261 1296, June 1998.
16. Roe, P. L.: Characteristic-Based Schemes for the Euler Equations. Annual Review of Fluid Mechanics, Volume 18, Milton van Dyke, J. V. Wehausen, and John L. Lumley, Eds. Annual Reviews Inc., 1986, pp. 337-365.
17. Spalart. P.R., Allmaras, S.R.: A One-Equation Turbulence Model for Aerodynamic Flows. AIAA Paper No. 1992-0439.
18. Biedron, R.T., Thomas, J.L.: A Generalized Patched-Grid Algorithm With Application to the F-18 Forebody With Actuated Control Strake. Comput. Sys. Eng., Vol. 1, nos. 2-4, 1990, pp. 563-576.
19. Bobbitt, C., Jr., Everhart, J.L., Foster J., Hill, J., McHatton, R., and Tomek, W.: National Transonic Facility Characterization Status. AIAA Paper No. 2000-0293, January 2000.
20. Iyer, V., Everhart, J.L., Bir, P.J., Ulbrich, N.: Implementation of WICS Wall-Interference Correction System at the National Transonic Facility. AIAA Paper No. 2000-2383, June 2000.

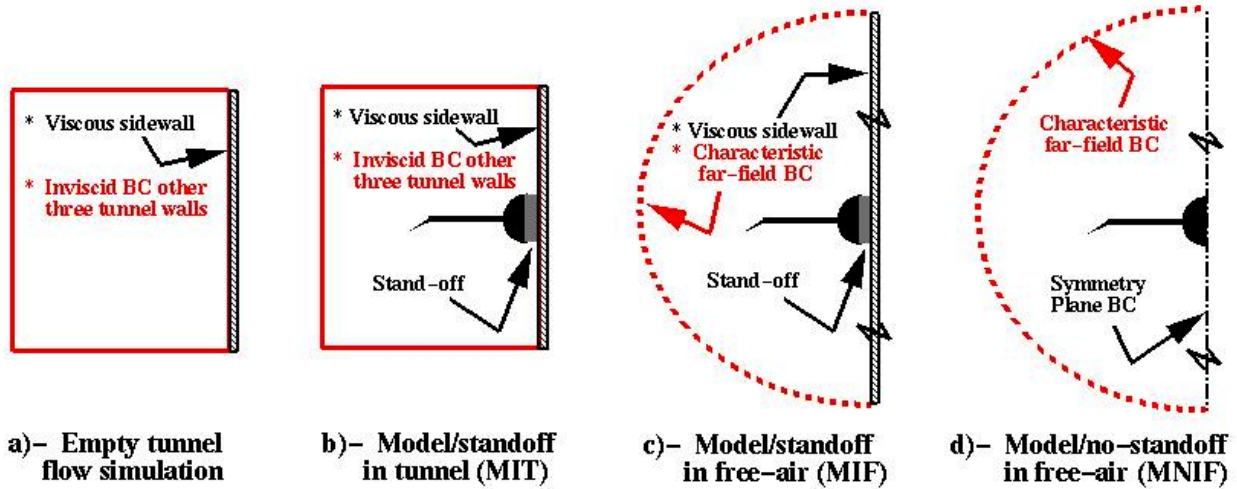


Figure 1. CFD plan for the NTF diamond wing semispan model.

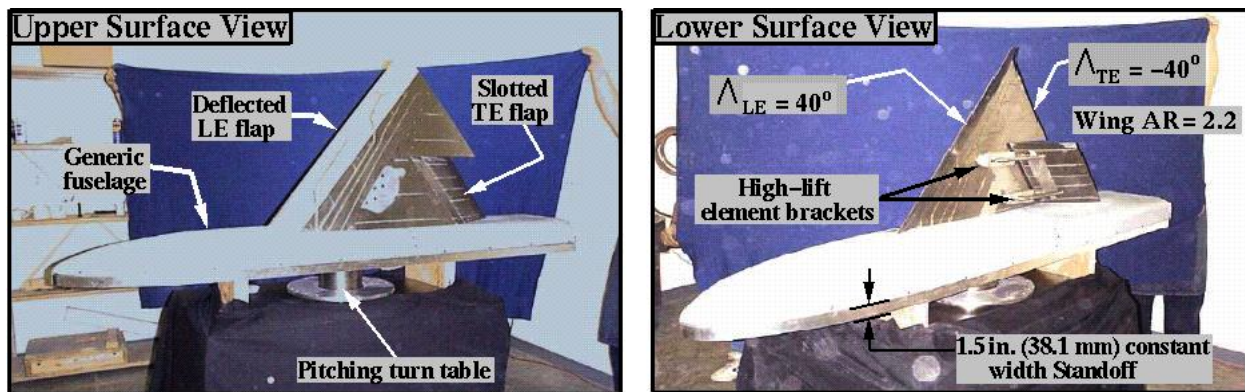


Figure 2. Diamond wing semispan model description.

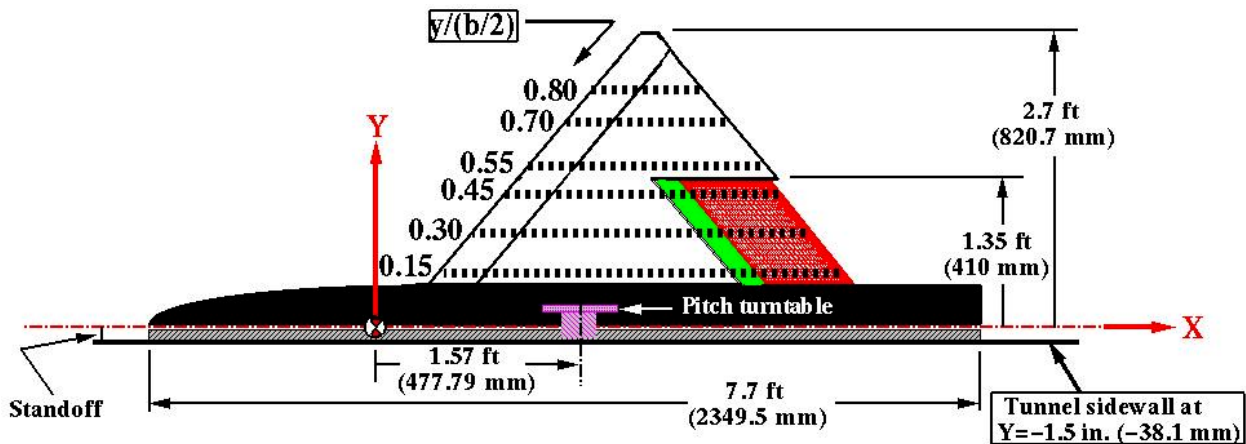


Figure 3. Schematic plan-form view of the model.

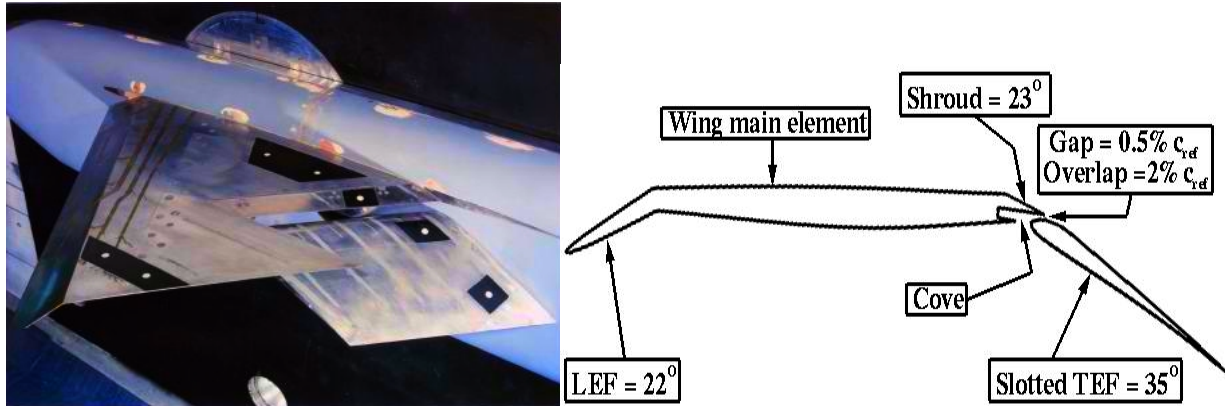


Figure 4. Diamond wing semispan model mounted on the NTF tunnel sidewall and a typical wing high-lift section.

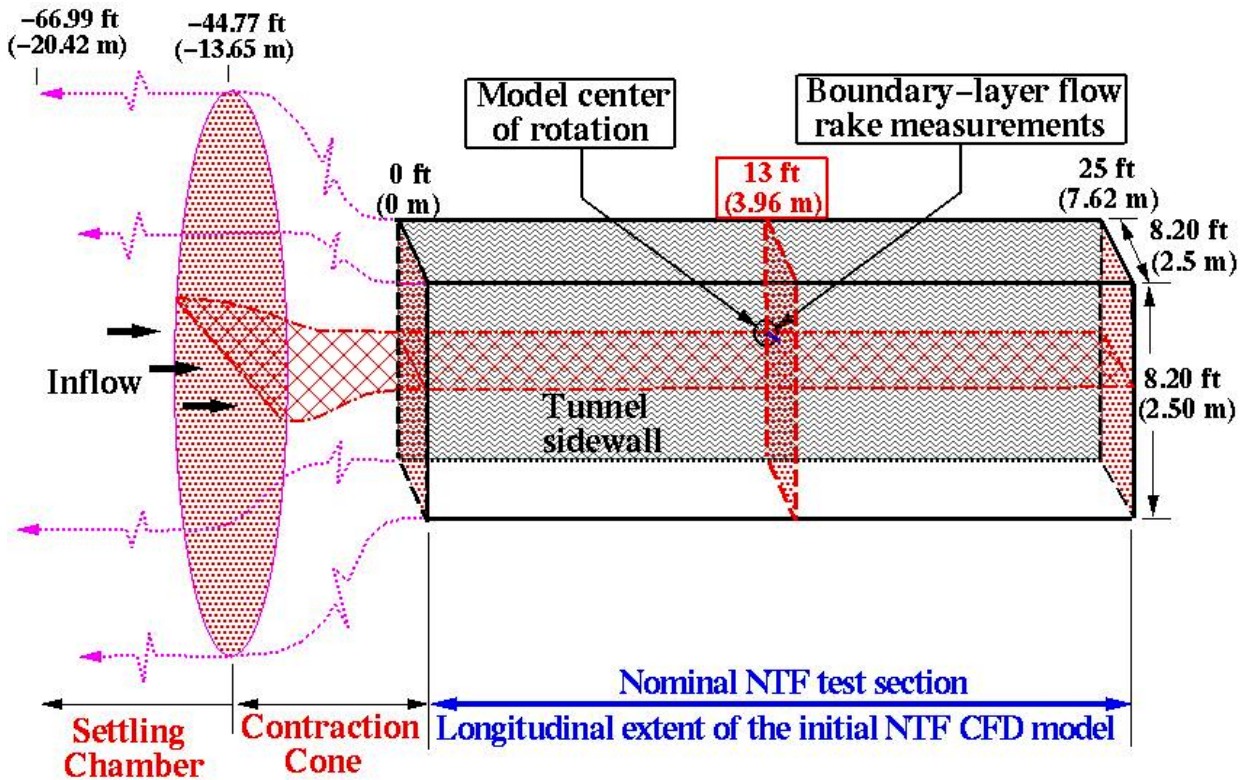


Figure 5. Schematic view of the NTF test section.

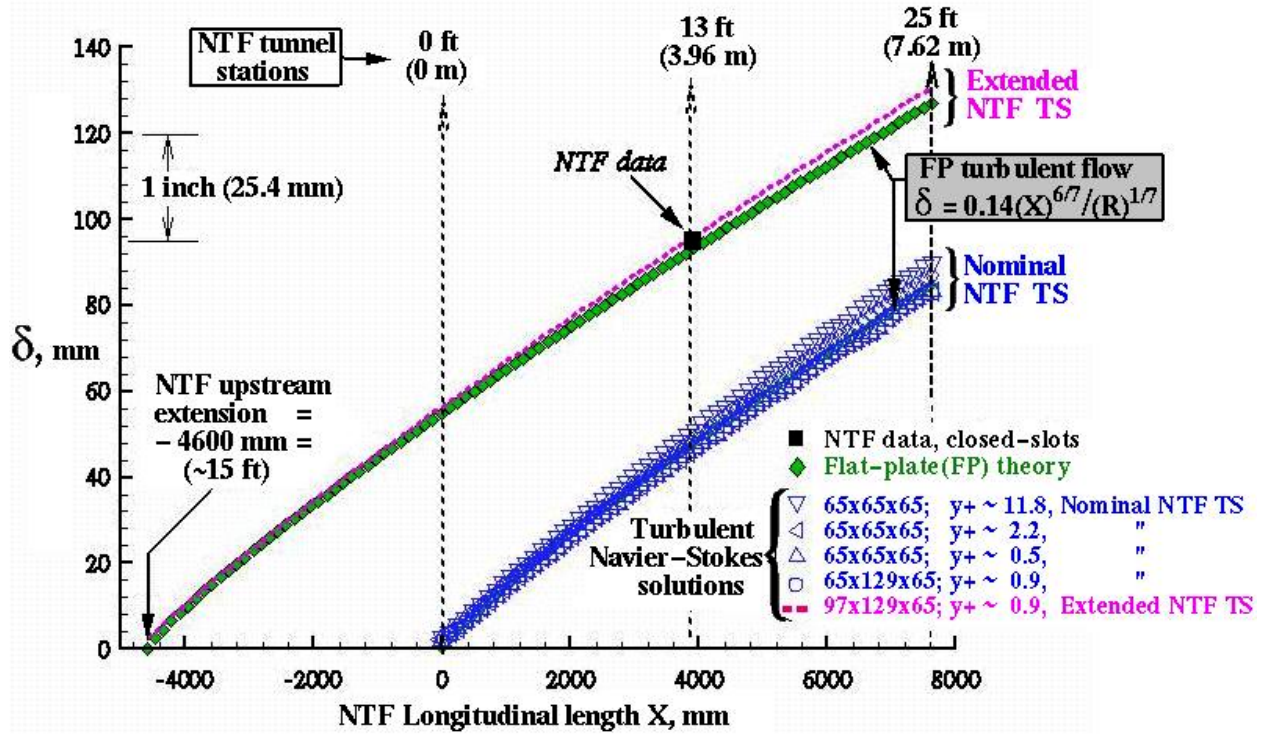


Figure 6. Computed Navier-Stokes, flat-plate theory and measured boundary-layer thickness-growth along NTF sidewall.

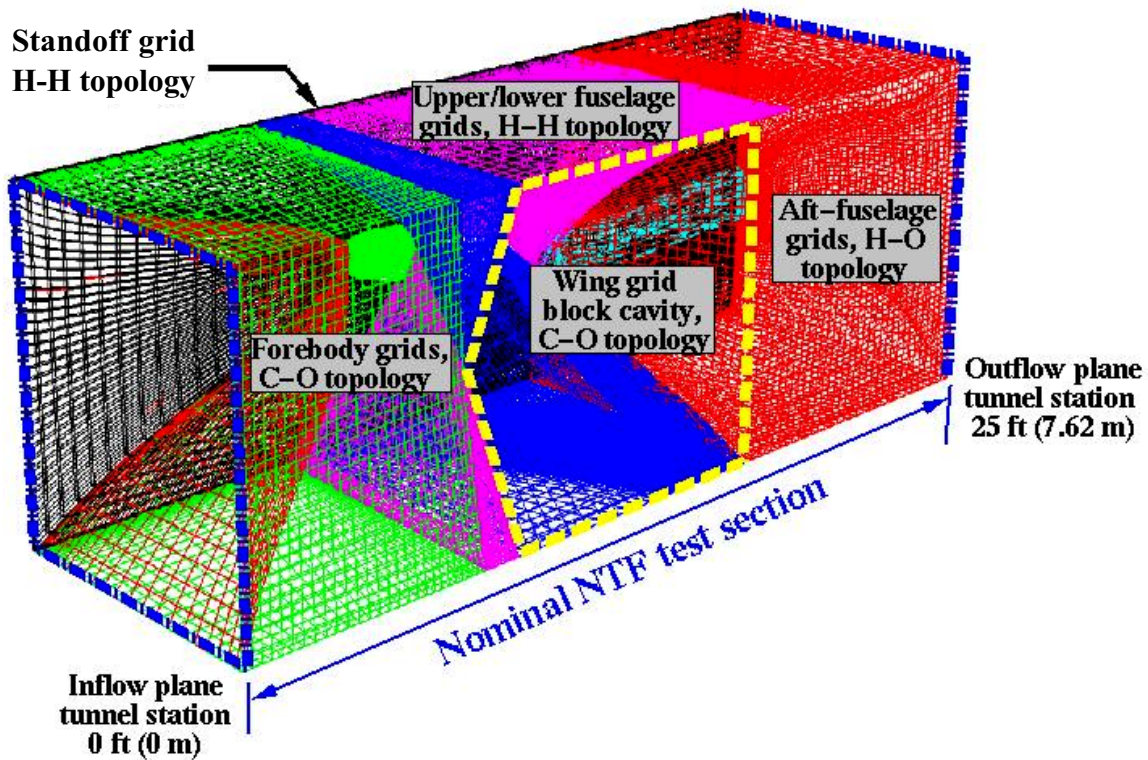


Figure 7. Grid topology for the Model/Stand-off in the nominal NTF test section.

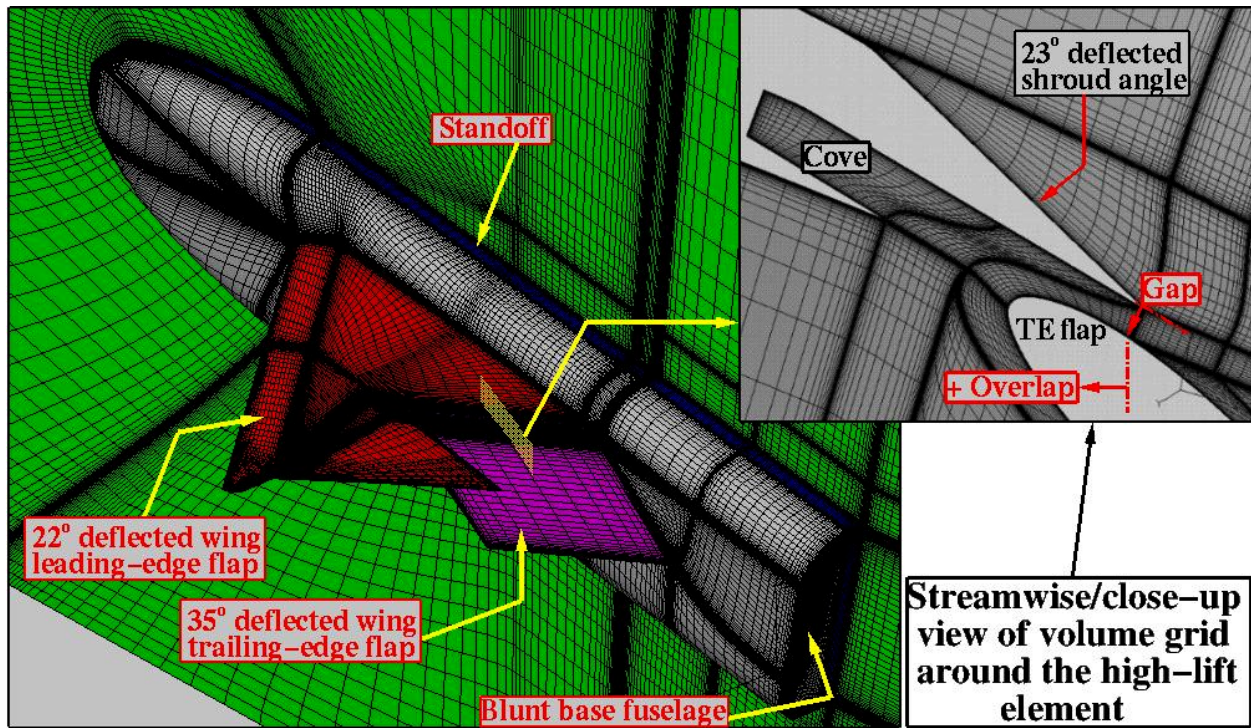


Figure 8. Close -up view of the semispan diamond wing numerical model mounted on the NTF tunnel

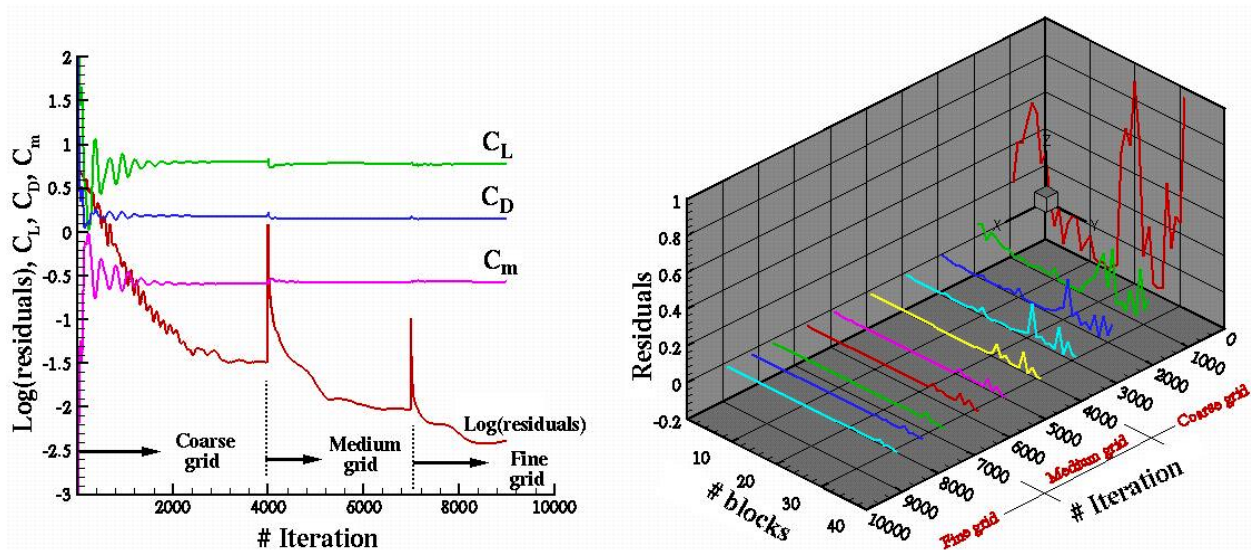


Figure 9. Solution convergence characteristics for MIT.

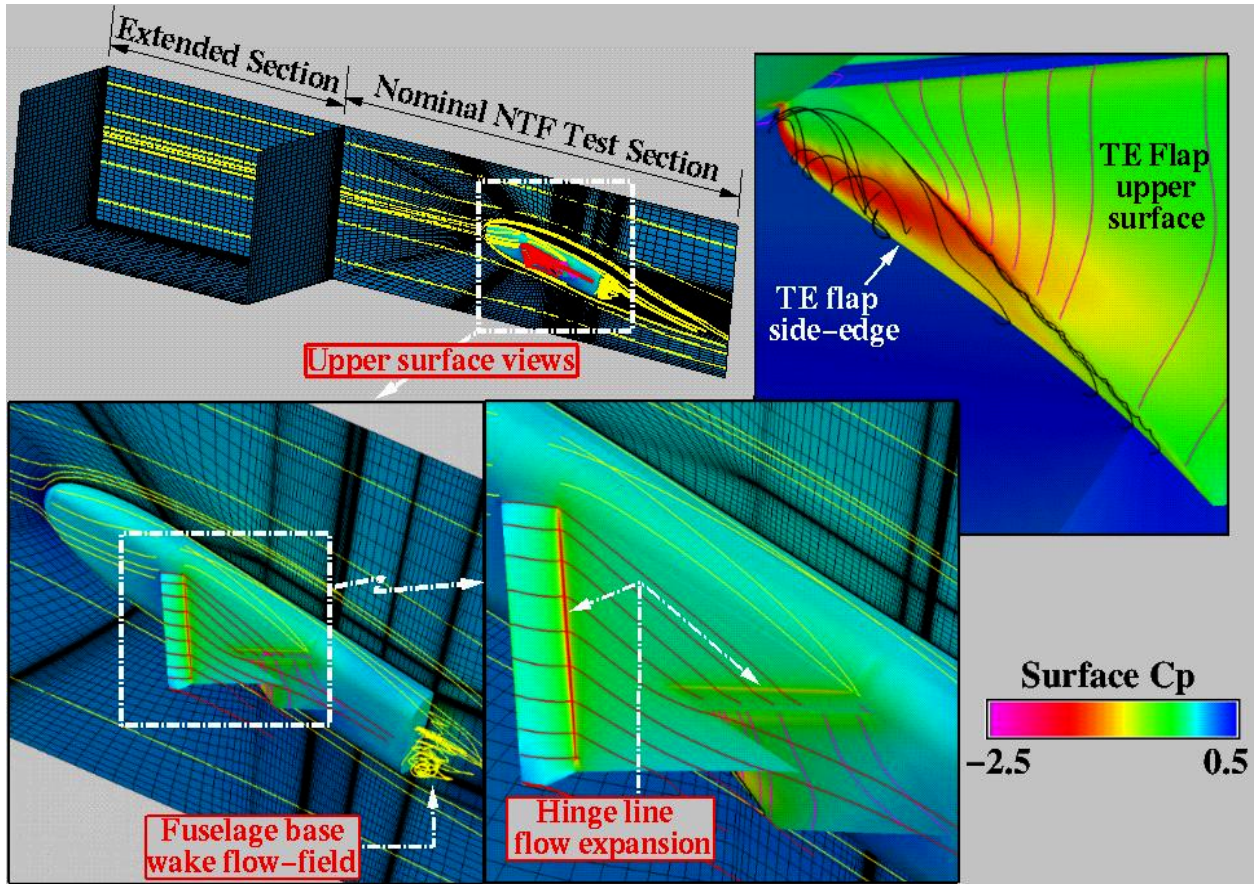


Figure 10. Turbulent Navier-Stokes flow field simulation for the semispan diamond wing in the extended NTF tunnel test section.

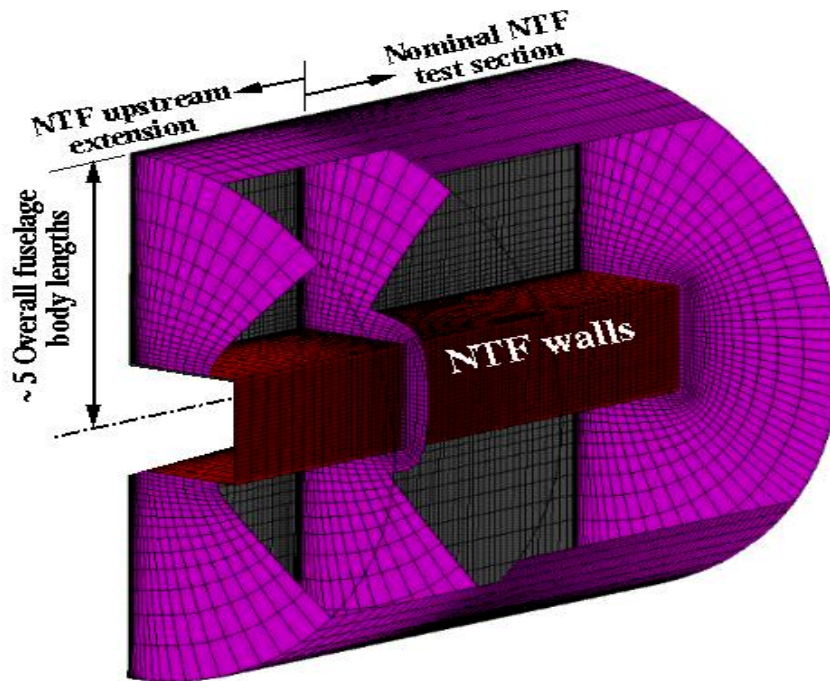


Figure 11. Exterior grid wrapping around the MIT grid for developing the MIF grid.

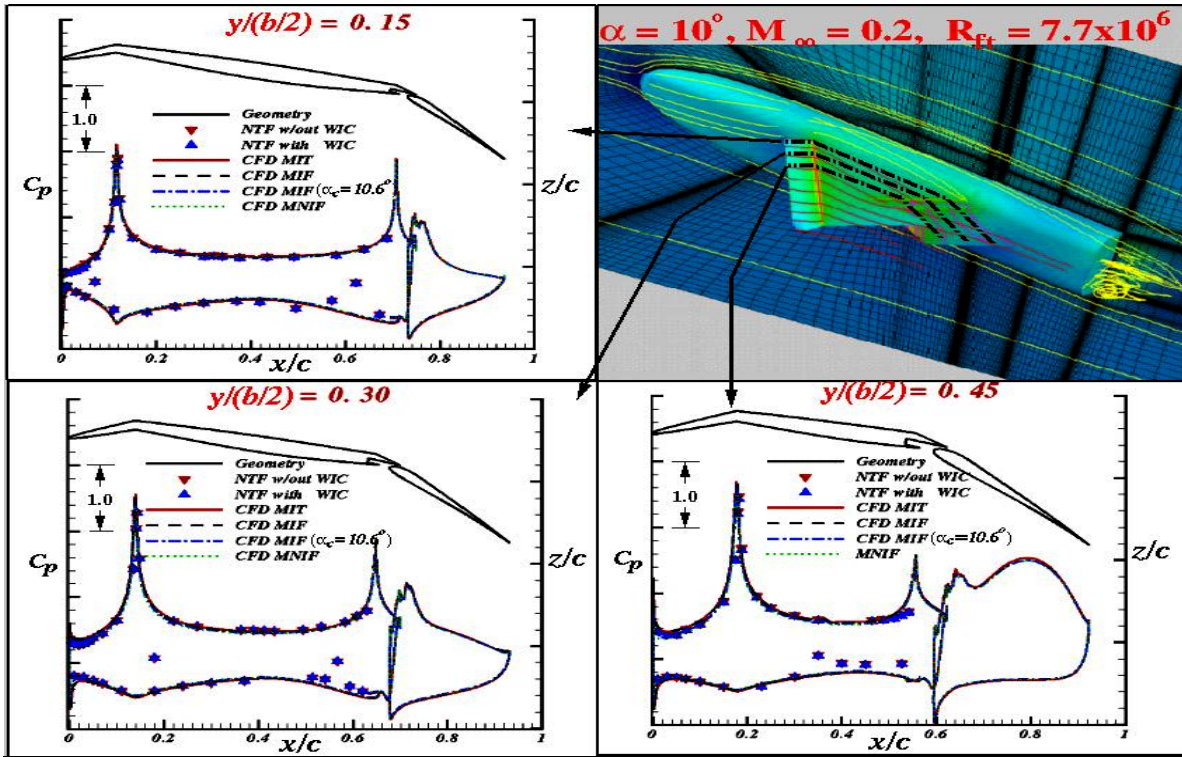


Figure 12. Computed surface pressures and correlation with data.

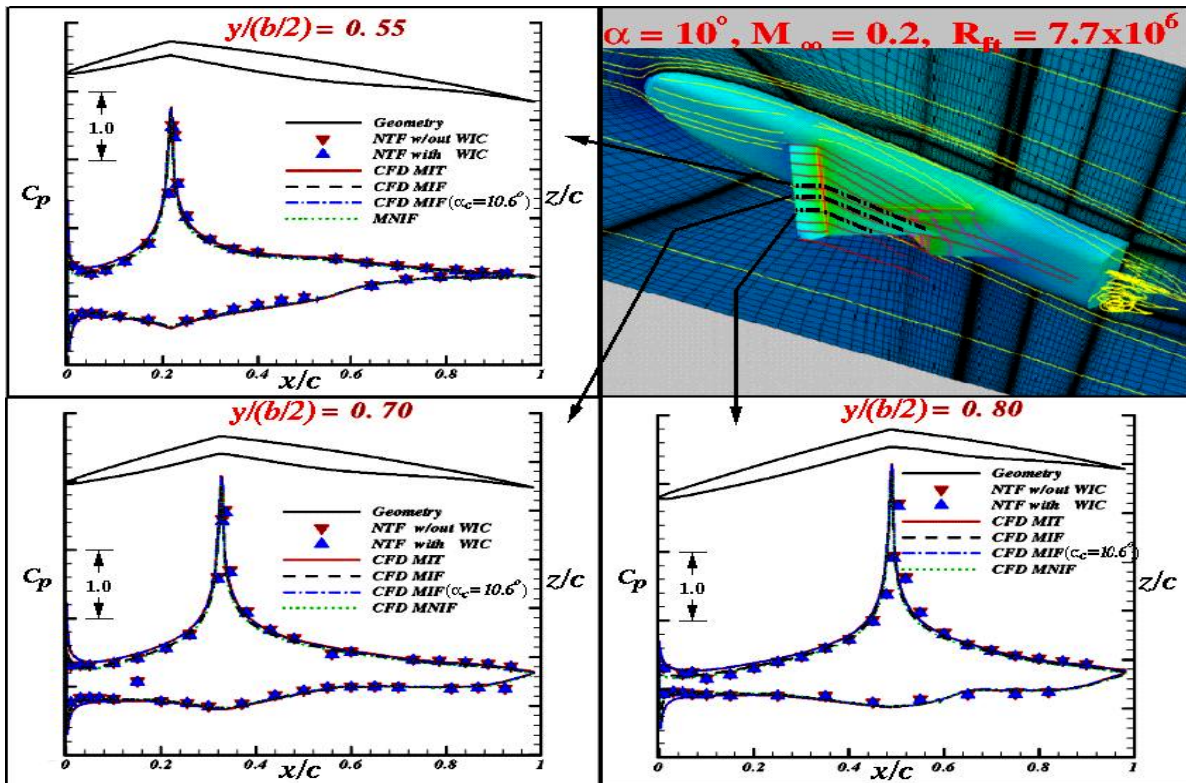


Figure 13. Computed surface pressure and correlation with data

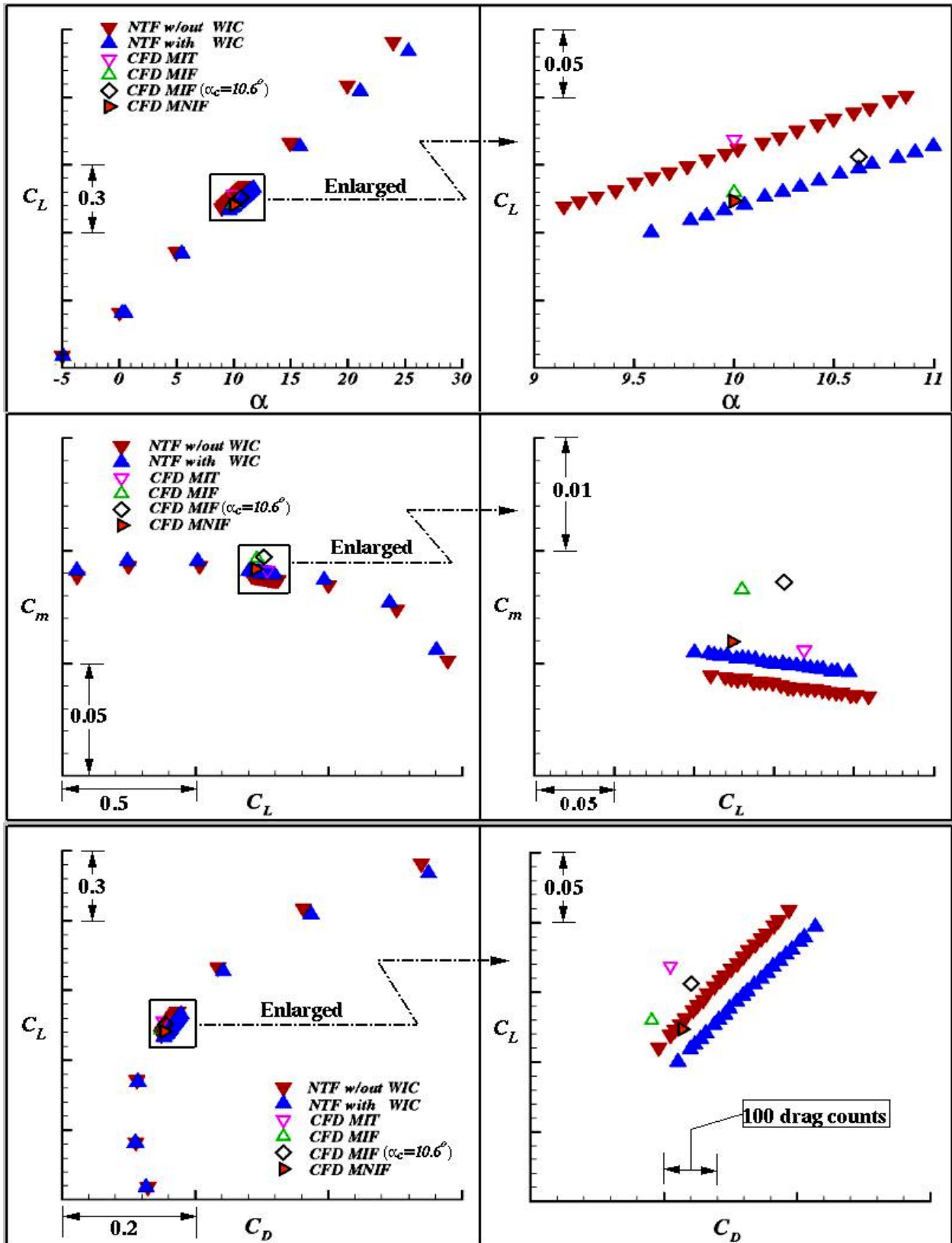


Figure 14. Computed and measured longitudinal aerodynamic characteristics.

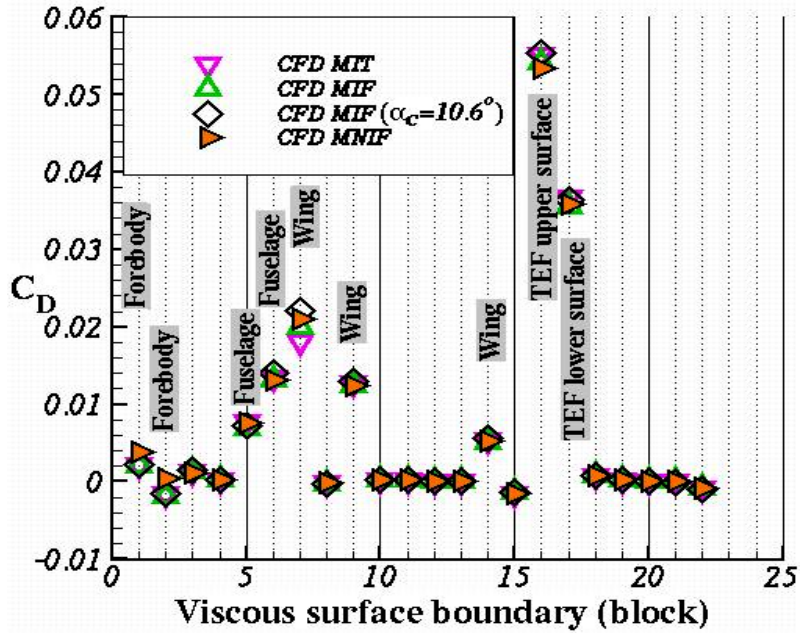


Figure 15. Computed drag coefficients for configuration various components (blocks).

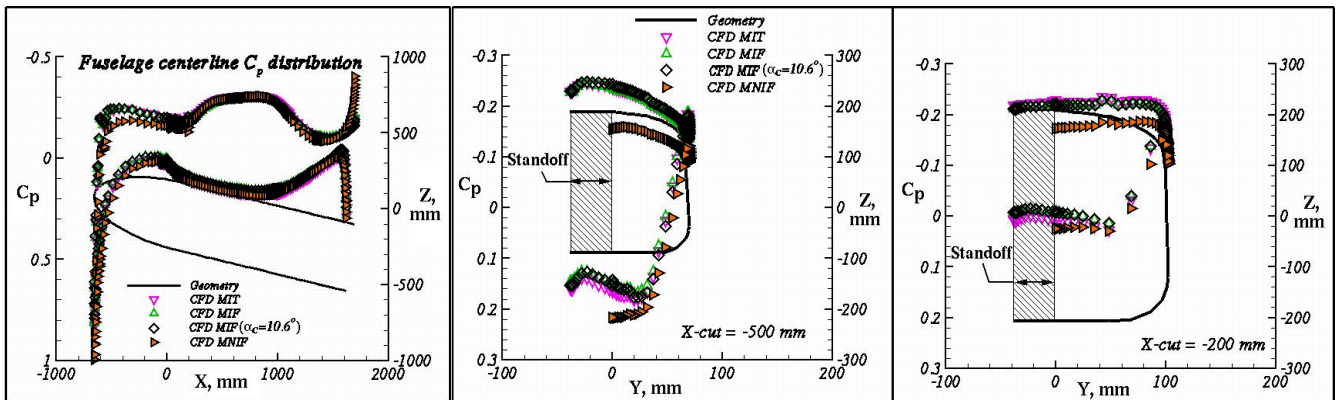


Figure 16. Computed C_p along the fuselage centerline ($Y=0$) and two forebody cross sections.

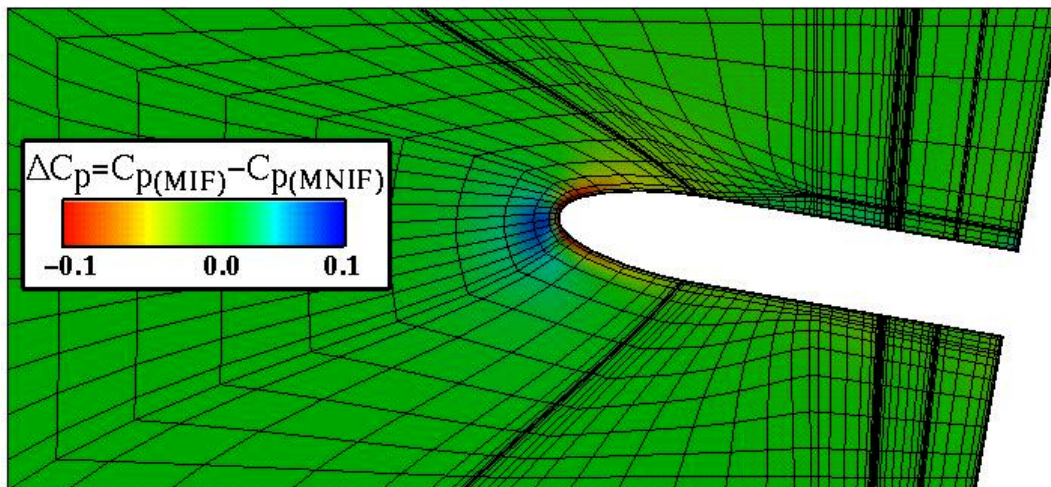


Figure 17. Computed pressure difference between MIF and MNIF along the fuselage center plane ($Y=0$).